RESEARCH ARTICLE

Energy & Environmental Materials WILEY

Magnesium Batteries

Confinement–Adsorption Synergy in Hybrid Carbon-Coated Separator Enables Stable High-Rate Quinone Cathode for Magnesium Batteries

*Xiquan Qi, Xingyu Gao, Zhirong Zhao-Karger, and Xiangyu Zhao**

Organic cathodes offer great promise for rechargeable magnesium batteries (RMBs) owing to their structural tunability and fast Mg^{2+} transport, yet their dissolution in ether-based electrolytes leads to rapid capacity fading and poor rate performance. Herein, we design a high-performance sulfur-containing heterocyclic quinone cathode, benzo[b]naphtho[2′,3′:5,6][1,4]dithiino[2,3-i]thianthrene-5,7,9,14,16,18-hexone (BNDTH), coupled with a functional carbon-coated separator composed of graphene oxide (GO) and carboxylated multi-walled carbon nanotubes (MWCNTs–COOH) at an optimized 1:9 mass ratio. In this architecture, GO provides physical confinement to suppress BNDTH diffusion, while MWCNTs–COOH offer abundant chemical adsorption sites to immobilize soluble species. This synergistic confinement–adsorption mechanism effectively mitigates active-material loss and promotes charge transfer. As a result, the Mg//BNDTH cell exhibits significantly improved rate capability, delivering cathode capacities rising from 153 to 261 mAh g^{-1} at 1 C and from 26 to 100 mAh g^{-1} at 10 C over 500 cycles, along with cell-level power and energy densities of 4517 W kg^{-1} and 222 Wh kg^{-1}, respectively—surpassing most reported RMBs employing organic cathodes. This work presents a viable separator-engineering strategy for achieving stable and high-rate operation of soluble organic cathodes in RMBs.

1. Introduction

Rechargeable magnesium batteries (RMBs) are gaining attention as a compelling next-generation energy storage technology, capitalizing on the intrinsic merits of magnesium metal anodes, including an ultrahigh volumetric capacity (3833 mAh cm^{-3}), superior safety, abundant reserves, and the propensity for uniform deposition over prolonged plating/stripping cycling.[1–11] Realizing high-performance RMBs, however, critically depends on the development of cathode materials capable of delivering both high energy and power densities—an ambitious target that requires the delicate balance of elevated operational voltages and high-specific capacities. Despite ongoing efforts, progress remains hindered by the limited availability of cathode materials that can meet these dual demands.[12] This limitation arises primarily from the strong coulombic interactions between divalent Mg^{2+} ions and inorganic host frameworks, which impose high migration energy barriers and restrict Mg^{2+} mobility within solid lattices.[13,14] The resulting sluggish solid-state diffusion kinetics undermine rate performance and capacity utilization.[15,16] Overcoming these intrinsic bottlenecks necessitates the rational design of cathode architectures with engineered ion transport pathways, capable of facilitating efficient Mg^{2+} migration while preserving structural stability under electrochemical cycling.

In this context, organic cathode materials have emerged as a compelling class of candidates, offering distinct advantages over traditional inorganic materials, including cost-effectiveness, environmental sustainability, structural diversity, and molecular-level redox tunability.[17–19] Unlike intercalation-based mechanisms in crystalline hosts, organic redox systems operate via functional group transformations, which facilitate multiple Mg^{2+} transport pathways and reduce intermolecular binding force, resulting in enhanced diffusion kinetics and electrochemical performance.[20] Among them, small-molecule organic electrodes exhibit high theoretical capacities and dense redox-active sites. However, their practical application is constrained by high solubility in conventional electrolytes, leading to severe capacity fading.[21,22] To mitigate this drawback, strategies such as molecular polymerization and separator modification have been proposed.[23–25] In the molecular polymerization approach, redox-active groups are covalently tethered onto linear or crosslinked polymeric backbones.[26] The resulting polymers, with enhanced molecular weights and intermolecular forces, exhibit significantly reduced solubility in electrolytes. For instance, while pristine anthraquinone suffers from rapid capacity loss (10 mAh g^{-1} after 30 cycles at 100 mA g^{-1}) due to severe dissolution,[27] anthraquinone-based polymers designed by Liao et al., including anthraquinonylsulfide, 1,4-polyanthraquinone, and 2,6-

X. Qi, X. Gao, Prof. X. Zhao
State Key Laboratory of Materials-Oriented Chemical Engineering, Jiangsu Collaborative Innovation Center for Advanced Inorganic Functional Composites, College of Materials Science and Engineering, Nanjing Tech University, Nanjing 211816, China
E-mail: xiangyu.zhao@njtech.edu.cn
Dr. Z. Zhao-Karger
Helmholtz Institute Ulm (HIU), Helmholtzstr. 11, D-89081, Ulm, Germany
Institute of Nanotechnology (INT), Karlsruhe Institute of Technology (KIT), P.O. Box 3640, D-76021, Karlsruhe, Germany
The ORCID identification number(s) for the author(s) of this article can be found under https://doi.org/10.1002/eem2.70295.

DOI: 10.1002/eem2.70295

polyanthraquinone, demonstrated improved cycling performance.[28] Xu et al. further developed a double-chain poly(anthraquinonylsulfide) with higher capacity and stability, delivering 194 mAh g^{-1} after 50 cycles at 100 mA g^{-1}.[21] Despite these advances, the sluggish Mg^{2+} diffusion within polymer matrices remains a fundamental challenge, as steric hindrance and strong ion–polymer interactions limit ionic mobility and degrade rate capability.

Separator modification has emerged as a highly efficient strategy to suppress the shuttle effect of dissolved organic species, thereby improving cycling stability. For example, Kang et al. reported a metal–organic framework (MOF) gel membrane separator for lithium−organic batteries, in which the intrinsic microporous architecture of the MOF functions as molecular sieves that selectively regulate the transport of soluble redox-active species. This design effectively suppresses the shuttle effect while preserving high-power density, enabling long-term cycling with 82.9% capacity retention after 2000 cycles.[29] Likewise, Jia et al. demonstrated that Super P-coated polypropylene separators, as a physical barrier, effectively restricted the diffusion of soluble quinone-based small molecules in sodium-based systems. Paired with a sodium metal anode, the dibenzo[b,i] thianthrene-5,7,12,14-tetraone cathode achieved an exceptional capacity of 342.6 mAh g^{-1} at 500 mA g^{-1} and maintained a low capacity fade rate of 0.15% per cycle over 550 cycles.[30] However, in the field of RMBs, separator modification strategies targeting the dissolution issue of organic cathodes remain largely unexplored.

Herein, we report a sulfur-containing heterocyclic quinone, benzo[b]naphtho[2′,3′:5,6][1,4]dithiino[2,3-i]thianthrene-5,7,9,14,16,18-hexone (BNDTH), as a high-capacity organic cathode for RMBs. Owing to its low molecular weight and high density of redox-active sites, BNDTH is well-suited for high-power Mg^{2+} storage. Nevertheless, its dissolution in electrolytes leads to rapid capacity degradation. To address this, we fabricated a hybrid carbon-coated separator via vacuum filtration of graphene oxide (GO) and carboxylated multi-wall carbon nanotubes (MWCNTs−COOH) onto commercial glass fiber film. By adjusting the mass ratio of GO to MWCNTs−COOH (1GO/xMWCNTs−COOH), an optimized 1GO/9MWCNTs–COOH coating was obtained, forming a compact and effective diffusion barrier for active species. This modified separator enabled the BNDTH cathode to deliver an average discharge voltage of 1.75 V (versus Mg/Mg^{2+}) and a high reversible capacity of 261 mAh g^{-1} at 1 C (295 mA g^{-1}). Notably, the cathode exhibits significantly improved rate performance with a capacity of 154 mAh g^{-1} at 10 C, while maintaining 100 mAh g^{-1} after 500 cycles.

2. Results and Discussion

2.1. Synthesis and Characterization of BNDTH

BNDTH was successfully synthesized via a straightforward condensation reflux method,[31] in which two naphthoquinone units and one benzoquinone unit are covalently linked, as illustrated in **Figure 1**a. BNDTH contains six carbonyl (C=O) groups serving as redox-active sites, endowing it with a high theoretical specific capacity of 295 mAh g^{-1}. X-ray powder diffraction (XRD) analysis of BNDTH shows distinct diffraction peaks (Figure 1b), indicative of a well-ordered crystalline structure that may provide continuous ion-diffusion pathways. Fourier transform infrared (FTIR) spectroscopy of BNDTH (Figure 1c) confirms its molecular structure, displaying characteristic absorption bands at 1662 and 1651 cm^{-1} corresponding to C=O stretching vibrations, and peaks at 1585 and 1536 cm^{-1} assigned to aromatic C=C stretching modes. A prominent absorption at 701 cm^{-1} is attributed to C–S bond vibrations, collectively validating the successful incorporation of redox-active carbonyl functionalities and sulfur-containing moieties into the molecular backbone of BNDTH. The chemical composition and bonding environment of BNDTH were further elucidated by X-ray photoelectron spectroscopy (XPS) (Figure S1, Supporting Information). Deconvolution of the C 1s spectrum (Figure 1d) reveals three distinct components centered at 284.8 eV (C–C/C=C), 286.2 eV (C–O/C–S), and 288.6 eV (C=O), while the O 1s spectrum (Figure 1e) displays two peaks at 531.4 eV (C=O) and 533.0 eV (C–O). The S 2p spectrum (Figure 1f) exhibits a well-defined doublet at 163.8 eV (S $2p_{3/2}$) and 165.0 eV (S $2p_{1/2}$), corroborating the presence of C–S bonds and confirming the designed molecular framework.

Solid-state ^{13}C nuclear magnetic resonance (NMR) spectroscopy (Figure 1g) provides additional structural validation, featuring a prominent resonance at ~170 ppm assigned to the carbonyl carbons of the quinone units. This direct observation of redox-active centers complements the XPS and FTIR results and confirms the high chemical purity of the synthesized BNDTH. These spectroscopic analyses collectively verify the rational molecular design of BNDTH, which integrates dual functionalities—redox-active carbonyl groups for Mg^{2+} coordination and sulfur bridges for structural robustness. The morphology of BNDTH was examined by scanning electron microscopy (SEM, Figure 1h), revealing uniform, monodisperse microrods with an average length of ~4 μm and ultrathin walls. Such well-defined one-dimensional structures shorten Mg^{2+} diffusion pathways and enhance ion transport kinetics. Energy dispersive spectroscopy (EDS) elemental mapping (Figure 1i) further verifies the homogeneous distribution of C, O, and S elements throughout the microrod matrix, in agreement with the designed sulfur-bridged quinone framework.

2.2. Electrochemical Performance and Redox Mechanism of BNDTH Cathode

The electrochemical performance of BNDTH was evaluated using CR2032-type coin cells assembled with magnesium metal as the anode and a non-corrosive electrolyte consisting of 0.5 M $Mg[B(hfip)_4]_2$ (hfip = $OC(H)(CF)_3)_2$ in 1,2-dimethoxyethane (DME). This electrolyte demonstrated excellent anodic stability above 3.5 V (versus Mg^{2+}/Mg) when carbon-coated aluminum (C–Al) or stainless steel was used as the working electrode, as confirmed by linear sweep voltammetry (LSV, Figure S2a, Supporting Information), thus supporting the use of high-voltage cathode materials. Furthermore, it enabled efficient Mg plating/stripping behavior in both symmetric Mg||Mg cells and asymmetric C–Al||Mg cells (Figure S2b–d, Supporting Information), indicating reversible Mg deposit and efficient Mg^{2+} transport throughout the electrolyte medium. Cyclic voltammetry (CV) of the BNDTH cathode (**Figure 2**a), conducted within the voltage window of 1.0–3.0 V, revealed two well-defined redox couples at 2.3/1.6 and 2.6/1.9 V, corresponding to the stepwise redox reactions between carbonyl (C=O) and ether (C–O) functional groups during Mg^{2+} storage. Notably, in the second and third cycles, an anomalous oxidation peak near 2.7 V emerged during the reduction sweep, which can be attributed to the partial dissolution of BNDTH in the electrolyte (Figure S3, Supporting Information). Galvanostatic charge/discharge profiles (Figure 2b) further corroborate the CV results, displaying two discharge plateaus at

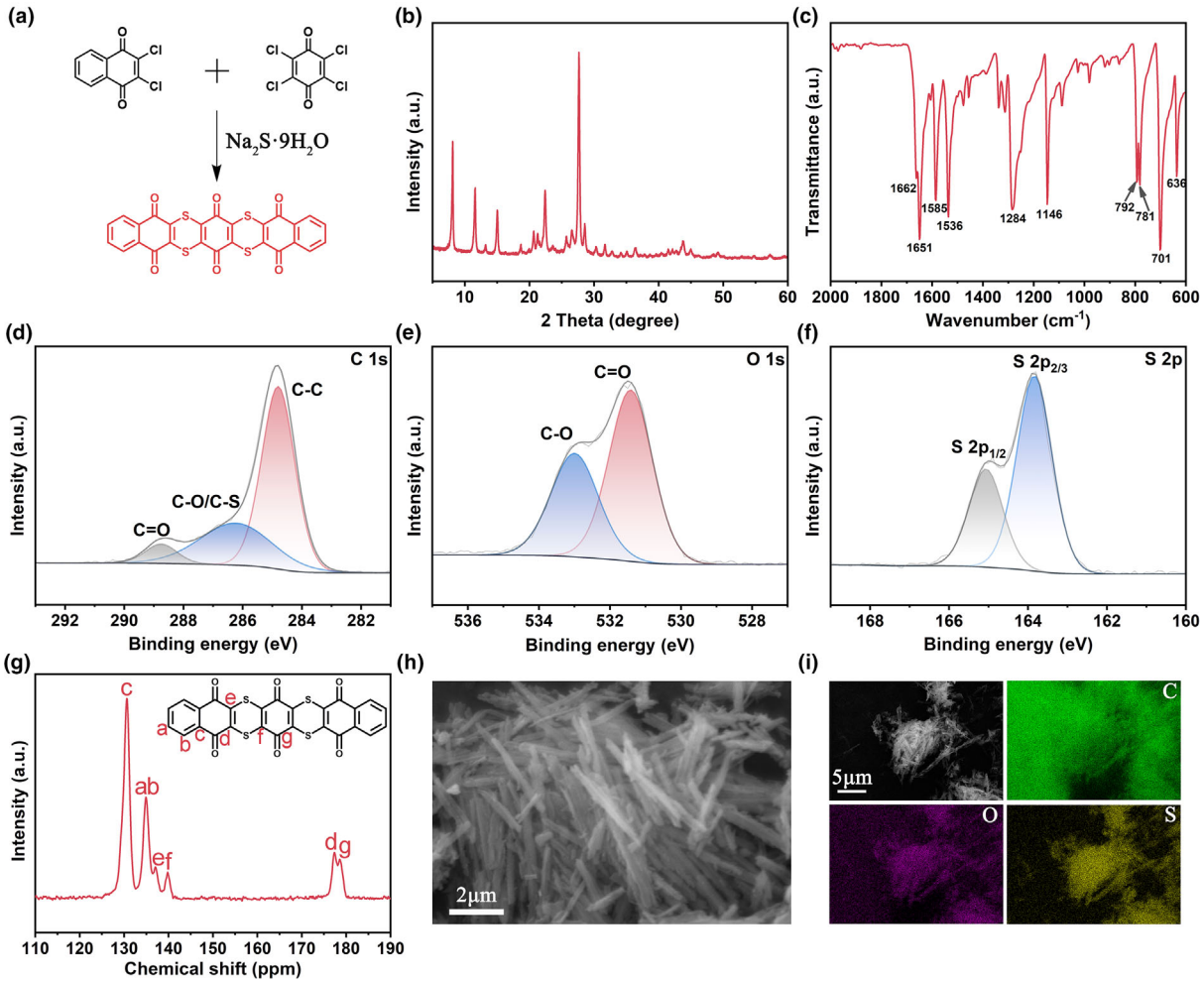

Figure 1. Structure analyses of BNDTH. a) Schematic illustration for the synthesis of BNDTH. b) XRD pattern and c) FTIR spectra of BNDTH. XPS spectra of BNDTH: d) C 1s, e) O 1s, and f) S 2p. g) Solid-state ^{13}C NMR spectrum of BNDTH. h) SEM images of BNDTH. i) EDS elemental mapping images of BNDTH.

1.9 and 1.6 V and delivering an initial capacity of 125 mAh g^{-1} at 1 C. However, continuous dissolution of active material led to a gradual decline in capacity to 77 mAh g^{-1} after 50 cycles.

Interestingly, the selection of binder was found to have a pronounced effect on the electrochemical behavior of the BNDTH cathode. To explore this effect, five different binders, carboxymethylcellulose (CMC), polyvinylidene fluoride (PVDF), sodium alginate (SA), polyacrylic acid (PAA), and acrylonitrile multi-copolymer (LA133), were evaluated under identical testing conditions. Among them, the BNDTH cathode using CMC binder exhibited the highest specific capacity and the best cycling stability at a current density of 100 mA g^{-1}, albeit with slightly lower coulombic efficiency compared to other binder systems (Figure S4, Supporting Information). This performance enhancement is further supported by the results of a tape-peeling test (Figure S5, Supporting Information), designed to assess the mechanical adhesion between the electrode coating and the current collector. Among all binder systems, the CMC-based electrode retained the largest amount of active material after peeling, significantly outperforming its PVDF- and other binder-based counterparts. Such strong interfacial adhesion likely contributes to maintaining the structural integrity and conductive network of the electrode during cycling, thereby improving its overall electrochemical stability. These results underscore the critical role of binder selection in optimizing the electrochemical performance of the BNDTH cathode.

To elucidate the redox mechanism of the BNDTH cathode, ex situ XRD, FTIR, and XPS analyses were conducted at different states of charge and discharge. Given the need for the initial electrochemical activation, the second cycle was selected to study the Mg^{2+} storage behavior of BNDTH. Ex situ XRD patterns of the BNDTH cathode reveal clear structural evolution during cycling (Figure 2c). Diffraction peaks at 24.2°, 38.5°, 44.9°, 58.4°, 65.5°, and 78.2° are assigned to the C–Al current collector. Upon discharge to 1 V, the characteristic BNDTH peak at 27.7° disappears, while a new peak emerges at 82.7°, indicating a phase transformation induced by Mg^{2+} insertion. When recharged to 3 V, the 27.7° peak is restored and the 82.7° peak vanishes, demonstrating the reversible crystalline reorganization of BNDTH associated with Mg^{2+} extraction.

To further probe the chemical bonding evolution, ex situ FTIR spectroscopy was performed (Figure 2d). The intensity of the C=O stretching vibration at 1650 cm^{-1} decreases upon discharge to 1 V and

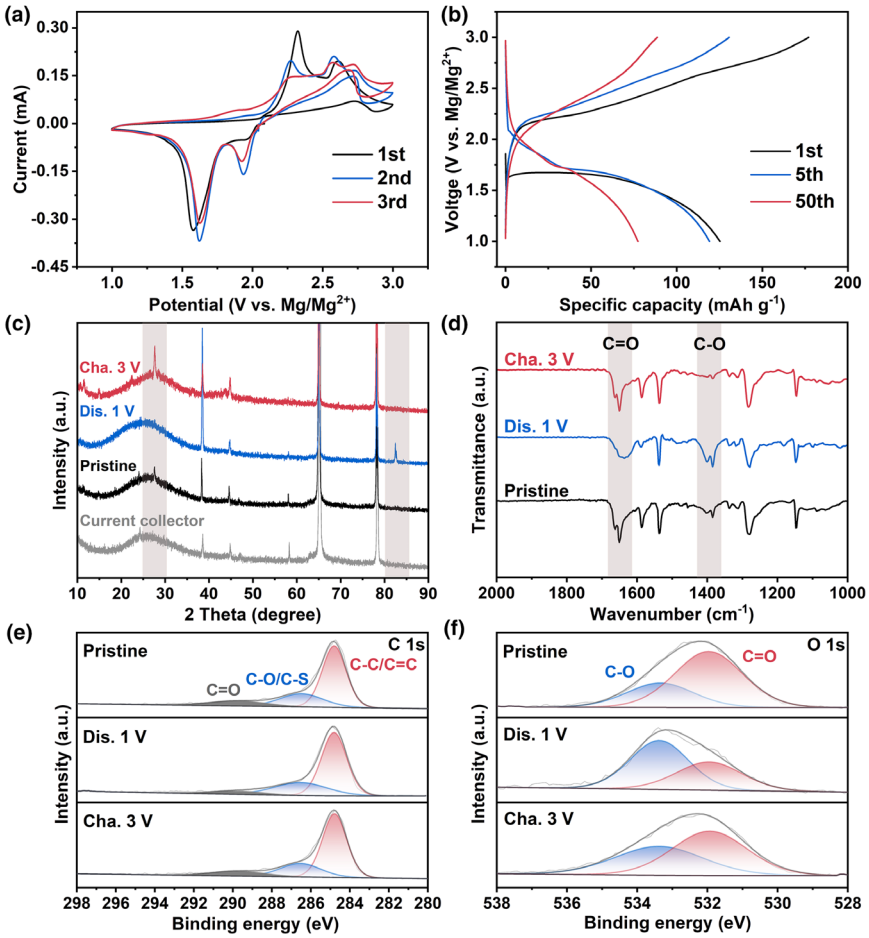

Figure 2. Electrochemical performance and redox mechanism of the BNDTH cathode. a) CV curves (0.1 mV s^{-1} and 1.0–3.0 V). b) Discharge/charge profiles of BNDTH at 1 C. c) Ex situ XRD patterns and d) ex situ FTIR spectra at different states in the 2nd cycle. Comparison of ex situ XPS spectra of e) C 1s and f) O 1s of pristine cathode and cathodes at different states in the 2nd cycle.

recovers after the recharge to 3 V, indicating the reduction and subsequent reoxidation of carbonyl groups. Meanwhile, the C–O stretching band at 1382 cm^{-1} becomes more pronounced during discharge and weakens during charge, consistent with the interconversion between C=O and C–O functionalities during Mg^{2+} coordination and release. These vibrational changes, in conjunction with XRD results, provide compelling evidence for the reversible structural evolution of BNDTH during cycling. Ex situ XPS analysis further clarifies the redox-active centers involved in the magnesiation/de-magnesiation process. The high-resolution C 1s spectrum of the pristine cathode (Figure 2e) shows three components at 284.8 eV (C–C/C=C), 286.3 eV (C–O/C–S), and 287.9 eV (C=O). Upon discharge to 1 V, the intensity of the C=O peak significantly diminishes, while the C–O/C–S component becomes more prominent, indicating the reduction of carbonyl groups. Upon recharge to 3 V, the C=O peak intensity is largely restored, confirming the reversibility of this redox transformation. Similarly, the O 1s spectra (Figure 2f) exhibit an increase in the C–O signal at 533.3 eV and a decrease in the C=O signal at 532.0 eV upon discharge, with the reverse trend observed upon charge. Together, these spectroscopic results reveal that carbonyl groups in BNDTH undergo reversible reduction to C–O states upon Mg^{2+} insertion and reoxidation during Mg^{2+} extraction. The dynamic conversion between C=O and C–O bonding states, accompanied by the restoration of the original crystalline phase, confirms that carbonyl moieties serve as the primary redox-active sites.

2.3. Design and Structural Characterization of the GO/MWCNTs−COOH Hybrid Interlayer

To suppress active material loss and mitigate the shuttle effect while enhancing BNDTH's electrochemical stability, a hybrid interlayer composed of GO and MWCNTs−COOH was constructed on the cathode-facing side of a commercial GF separator. As shown in **Figure 3a**, ethanol-based suspensions with varying GO/MWCNTs−COOH mass ratios (1GO/xMWCNTs−COOH) were prepared via 4 h ultrasonication to obtain homogeneous dispersions. These were subsequently vacuum filtrated onto GF separators to form 1GO/xMWCNTs−COOH-coated separators. The as-prepared hybrid carbon interlayers exhibit outstanding mechanical robustness (Figure 3b), retaining structural integrity during repeated bending cycles. This durability stems from the synergistic reinforcement between the fibrous MWCNTs−COOH network and the planar GO sheets, which act as bridges across nanotube junctions, improving interfacial adhesion and crack resistance. In contrast, separators coated with only MWCNTs−COOH fractured severely during bending (Figure S6, Supporting Information), confirming GO's essential role in enhancing the interlayer's mechanical properties. Raman spectroscopic (Figure 3c) confirmed the formation of the hybrid carbon network, with characteristic D and G bands corresponding to disordered sp^3 and graphitic sp^2 carbon domains. A systematic upshift of the G-band from 1581 to 1591 cm^{-1} across the 1GO/xMWCNTs−COOH series reflects increased GO content, attributable to strengthened π-π stacking and strain transfer between the two carbonaceous components. Surface and cross-sectional SEM images (Figure 3d–k) reveal the microstructural evolution of the hybrid carbon interlayer. The pure MWCNTs−COOH layer (Figure 3d,e) forms an isotropic entangled fibrous mat (~50 μm thickness), while increasing GO content leads to ordered lamellar stacking. In the optimized 1GO/9MWCNTs−COOH configuration (Figure 3f,g), MWCNTs−COOH are uniformly anchored on GO basal planes, forming an interpenetrating architecture. Higher GO ratios (Figure 3h–k) enhance lamellar stacking but reduce conductive network connectivity. The hierarchical multilayer structure effectively prolongs electrolyte diffusion pathways and improves adsorption capacity for soluble BNDTH species, thus suppressing their migration toward the anode. Meanwhile, MWCNTs−COOH provide interconnected pathways for electrolyte infiltration and facilitate the retention of dissolved species within the hybrid carbon interlayer.

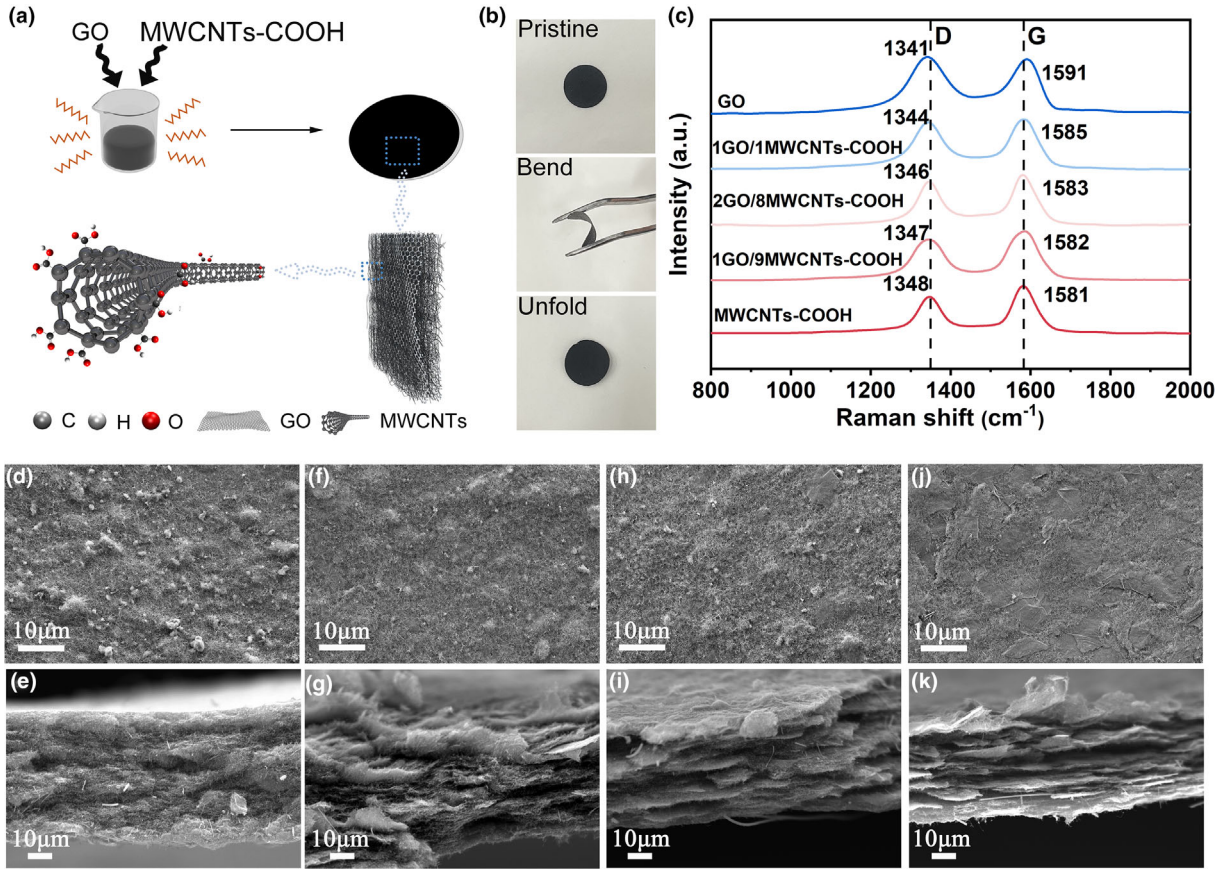

Figure 3. Morphology and structure of the functional GO/MWCNTs−COOH hybrid membrane. a) Schematic illustration for the synthesis of GO/MWCNTs−COOH hybrid carbon membranes and b) Optical photos of GO/MWCNTs−COOH hybrid carbon membrane in different states. c) Raman spectra of composite membranes with different GO/MWCNT−COOH ratios. Surface (d, f, h, j) and cross-sectional (e, g, i, k) SEM images of carbon membranes with different GO/MWCNTs−COOH ratios: MWCNTs−COOH, 1:9, 2:8, and 1:1.

2.4. Enhanced Electrochemical Performance of BNDTH Cathode with a GO/MWCNTs−COOH Modified Separator

Mg//BNDTH cells equipped with these carbon-modified separators exhibited significantly improved electrochemical performance compared to those using pristine GF separators. Among them, the GO/MWCNTs−COOH hybrid interlayer effectively regulates the shuttle of dissolved BNDTH species without altering its inherent redox chemistry, as evidenced by the nearly identical CV profiles (**Figure 4**a and Figure S7, Supporting Information). This confirms that the fundamental carbonyl-enolization redox pathway of BNDTH remains intact despite interfacial modification. However, a closer inspection of the CV data reveals composition-dependent variations in redox behavior. For instance, the Mg//BNDTH cell using the 1GO/1MWCNTs−COOH modified separator exhibits parasitic oxidative features near 2.7 V during the cathodic sweep (Figure S7a, Supporting Information), indicating incomplete suppression of BNDTH dissolution. Similar anomalies are observed in cells using 2GO/8MWCNTs−COOH and MWCNTs−COOH interlayers (Figure S7b,c, Supporting Information). Remarkably, these undesired redox signals are fully suppressed in the 1GO/9MWCNTs−COOH configuration, which simultaneously shows increased redox peak currents (Figure 4a), indicating an optimal balance between adsorption capacity and ionic/electronic transport kinetics. These findings establish the critical role of MWCNTs−COOH in adsorbing dissolved BNDTH species, while GO contributes to structural regulation of the hybrid carbon interlayer. The multilamellar architecture formed through appropriate GO incorporation offers efficient diffusion modulation and enhanced adsorption via physical confinement. However, excessive GO content negatively impacts the percolative electronic network, despite its contribution to barrier properties. This trade-off underscores the importance of the GO to MWCNTs−COOH ratio to maximize interlayer functionality.

The galvanostatic discharge and charge results further corroborate the above observations. The BNDTH cathode using the 1GO/9MWCNTs–COOH modified separator delivers a high first-cycle discharge capacity of 253 mAh g^{-1} (86% of theoretical capacity) at 1 C and retains 198 mAh g^{-1} after 50 cycles (Figure 4b), with an average discharge voltage of 1.75 V versus Mg/Mg^{2+}.

In contrast, the BNDTH cathode with other carbon-coated separators (Figure S8, Supporting Information) exhibits inferior metrics. The capacity contribution from the 1GO/9MWCNTs–COOH interlayer itself is shown in Figure S9, Supporting Information, confirming its negligible direct capacity. Extended cycling performance (Figure S10, Supporting Information) further highlights the efficacy of shuttle suppression. The BNDTH cathode coupled with the 1GO/9MWCNTs–COOH interlayer achieves a maximum discharge capacity of 261 mAh

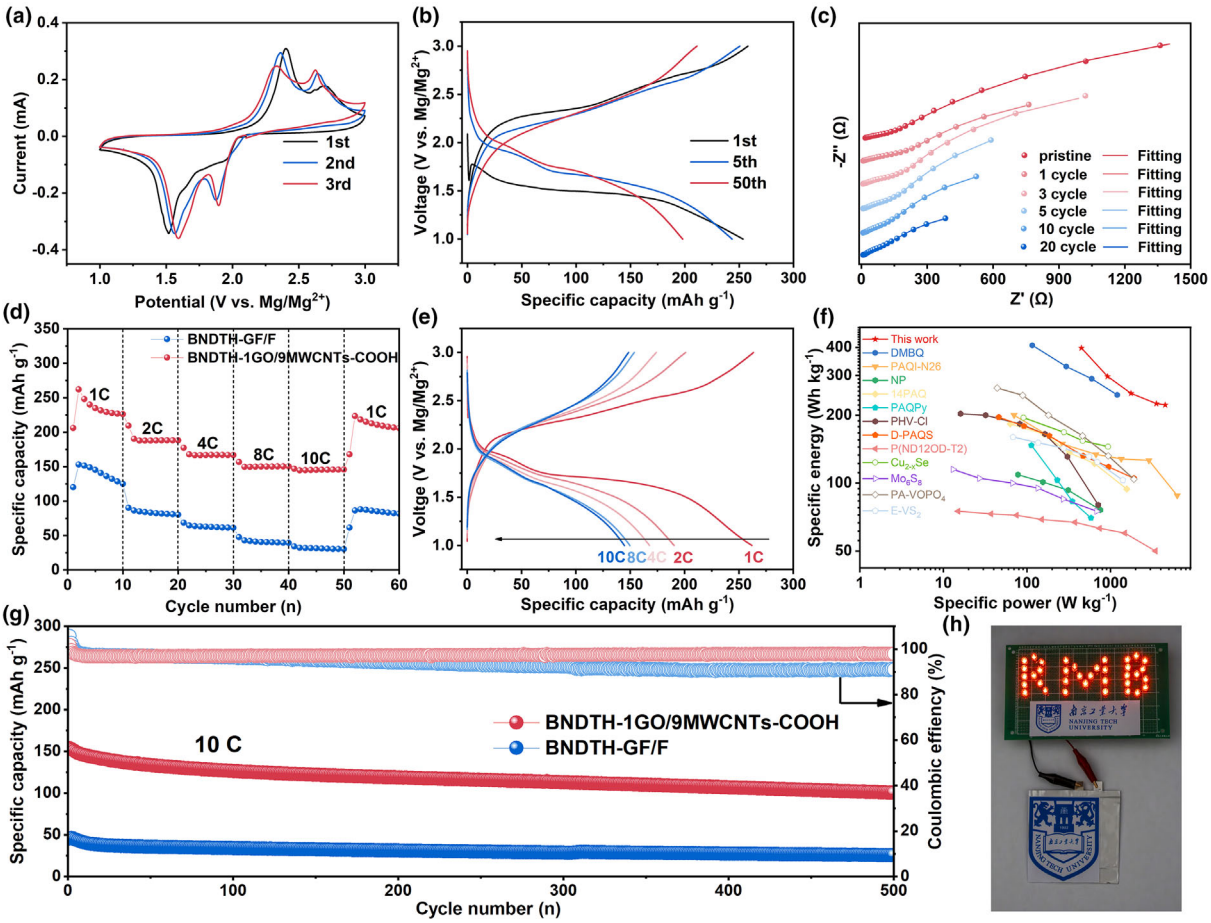

Figure 4. Electrochemical performances of Mg//BNDTH cells with 1GO/9MWCNTs–COOH modified separator. a) CV curves (0.1 mV s^{-1} and 1.0–3.0 V) and b) charge and discharge curves of BNDTH with 1GO/9MWCNTs–COOH modified separator at 1 C. c) EIS data comparison for the cell with 1GO/9MWCNTs–COOH modified separator at the pristine state and charged states after 1, 3, 5, 10, and 20 cycles. d) Rate performance from 1 to 10 C of the BNDTH with GF/F separator and BNDTH with 1GO/9MWCNTs–COOH modified separator. e) Charge and discharge profiles of BNDTH with 1GO/9MWCNTs–COOH modified separator at different current densities. f) Ragone plot of BNDTH and representative cathodes of RMBs (DMBQ,[32] PAQI-N26,[33] NP,[34] 14PAQ,[28] PAQPy,[23] PHV-Cl,[35] D-PAQS,[21] P(ND12OD-T2),[36] $Cu_{2-x}Se$,[37] Mo_6S_8,[38] PA-$VOPO_4$,[39] E-VS_2[40]). g) Long-term cycling performance at 10 C of the BNDTH with GF/F separator and 1GO/9MWCNTs–COOH modified separator. h) Image of 36 red LEDs powered by the soft-packing RMB.

g^{-1} at 1 C and retains 165 mAh g^{-1} (63.2% capacity retention) after 200 cycles. Comparatively, the cathode coupled with MWCNTs−COOH, 2GO/8MWCNTs–COOH, and 1GO/1MWCNTs–COOH interlayers exhibit maximum discharge capacities of 195, 214, and 199 mAh g^{-1} at 1 C and retain 94, 134, and 111 mAh g^{-1} after 200 cycles, respectively. These results collectively validate the superior adsorption capability and shuttle suppression effect of the 1GO/9MWCNTs–COOH hybrid interlayer.

Electrochemical impedance spectroscopy (EIS) further reveals insights into the reaction kinetics, with equivalent circuit and fitted parameters summarized in Tables S1–S5, Supporting Information. For the 1GO/9MWCNTs–COOH configuration, both the solution resistance (R_0) and charge transfer resistance (R_{ct}) decrease significantly (Figure 4c) during initial cycling due to improved electrolyte wetting and ionic transport across the BNDTH electrode and modified separator. While R_0 stabilizes in subsequent cycles, R_{ct} continues to decline, indicating enhanced charge transfer kinetics and reduced polarization. A minor R_{ct} increase observed in cycle 3 compared to cycle 1 is attributed to the intrinsically insulating property of GO, which slightly impedes electron transfer. Additional EIS results for other separators (Figure S11, Supporting Information) and corresponding R_0/R_{ct} values provide further comparison. Cells with 2GO/8MWCNTs–COOH and 1GO/1MWCNTs–COOH modified separators exhibit higher R_{ct} values than the 1GO/9MWCNTs–COOH system, although they follow a similar downward trend. This inverse correlation between GO content and electrochemical kinetics highlights the detrimental effects of excessive GO. Interestingly, the MWCNTs−COOH-only interlayer-based cell displays lower R_{ct} than the 1GO/9MWCNTs–COOH-based cell after several cycles, indicating favorable reaction kinetics, which may be ascribed to the enhanced active sites of pure MWCNTs−COOH interlayer compared to the hybrid interlayers. However, its relatively loose structure and highly porosity result in higher R_0 values, likely caused by diminished interfacial contact. In contrast, cells with unmodified GF separators maintained relatively stable but higher R_{ct} value, indicating

sluggish reaction kinetics. Collectively, these EIS findings confirm that the 1GO/9MWCNTs–COOH hybrid interlayer facilitates an optimal balance of ionic accessibility, electronic conductivity, and shuttle suppression, thereby substantially improving the electrochemical kinetics of the Mg//BNDTH cell. This kinetic enhancement underpins the superior rate capability and long-term cycling performance detailed below.

The BNDTH cathode incorporating the 1GO/9MWCNTs–COOH modified separator exhibits outstanding rate capability across a wide current rate range from 1 to 10 C (Figure 4d,e), delivering reversible capacities of 261, 190, 168, 150, and 145 mAh g^{-1} at respective current rates. Remarkably, when the current rate returns to 1 C after 50 high-rate cycles, the capacity retains at 225 mAh g^{-1}, reflecting good capacity recovery and structural reversibility. In sharp contrast, control cells using unmodified GF separators deliver substantially lower cathode discharge capacities under identical conditions (Figure 4d and Figure S12, Supporting Information). These enhanced electrochemical characteristics stem from the synergistic combination of BNDTH's multiple active sites with rapid redox kinetics and the modified separator's effective adsorption of dissolved BNDTH species. A comparative analysis of energy and power densities (Figure 4f and Table S6, Supporting Information) highlights the superior performance of the Mg//BNDTH cell, which achieves an impressive specific power of 4517 W kg^{-1} while maintaining a high energy density of 222 Wh kg^{-1} (calculated based on active materials of both cathode and anode), thereby demonstrating an excellent balance between power and energy output. These values not only establish BNDTH as a highly promising organic cathode but also validate the functional interlayer strategy for mitigating active material dissolution in RMBs. Notably, the 1GO/9MWCNTs–COOH modified system also demonstrates exceptional long-term cycling stability at 10 C (2950 mA g^{-1}), delivering a maximum capacity of 154 mAh g^{-1} and maintaining 100 mAh g^{-1} after 500 cycles (Figure 4g). This performance starkly contrasts with the GF-based cell, which exhibits only 46 mAh g^{-1} initial capacity and 26 mAh g^{-1} after cycling. These results strongly support the modified separator's efficacy in adsorbing dissolved BNDTH species and stabilizing cell operation over prolonged cycling. Furthermore, a soft-packed Mg//BNDTH cell assembled with the 1GO/9MWCNTs–COOH modified separator successfully powered 36 commercial red light-emitting diodes (LED, Figure 4h), demonstrating its potential for practical applications.

2.5. Synergistic Confinement–Adsorption Mechanism of the Hybrid Carbon Interlayer

To further elucidate the role of the hybrid carbon interlayer in mitigating BNDTH dissolution, adsorption experiments were conducted using the BNDTH solutions containing various hybrid carbon materials. Initial tests revealed that BNDTH exhibits pronounced solubility in DME, forming a saturated yellow solution upon immersion—accounting for severe capacity fading and poor rate performance of Mg//BNDTH cells. About 20 mg of GO/MWCNTs−COOH blends with varied mass ratios were introduced into saturated BNDTH/DME solutions. Over a 24 h immersion period, a gradual decolorization of the solutions was observed (**Figure 5a**). Notably, MWCNTs−COOH exhibited the most effective adsorption, completely clarifying the solution, whereas the 1GO/1MWCNTs−COOH composite showed minimal adsorption ability, with a large portion of the original coloration retained. To quantitatively evaluate adsorption capacity, UV–Vis spectroscopy was performed (Figure 5b). The absorbance results mirrored the visual observations, indicating an adsorption hierarchy of MWCNTs−COOH > 1GO/9MWCNTs−COOH > 2GO/8MWCNTs−COOH > 1GO/1MWCNTs−COOH. These findings underscore the dominant contribution of MWCNTs−COOH in BNDTH sequestration, consistent with macroscopic adsorption behavior. However, electrochemical performance analysis revealed an inverse correlation: although the MWCNTs−COOH-only interlayer exhibited the strongest adsorption capacity, cells using this separator underperformed relative to those with 1GO/9MWCNTs−COOH. This performance gap is primarily attributed to the poor mechanical integrity of the pure MWCNTs−COOH interlayer (Figure S6, Supporting Information), along with elevated ohmic resistance observed during cycling. This interlayer permits rapid diffusion of BNDTH across the membrane. In such cases, the dissolved BNDTH may traverse the interlayer before being efficiently adsorbed, thereby undermining the function of the MWCNTs−COOH. In contrast, the 1GO/9MWCNTs−COOH interlayer achieves a well-balanced synergy between structural confinement and adsorption capability. In this architecture, the GO sheets assemble into a densely stacked, layered structure that acts as a physical diffusion barrier. This compact configuration effectively retards the migration of dissolved BNDTH molecules, allowing sufficient residence time for the conductive MWCNTs−COOH network to capture the migrating BNDTH species. Nonetheless, excessive GO incorporation negatively affects cell performance through two mechanisms: 1) diminished BNDTH adsorption capacity due to the relatively inert GO surface and 2) reduced electrical conductivity caused by GO's intrinsically insulating nature. Therefore, the 1GO/9MWCNTs−COOH hybrid interlayer achieves an optimized balance between adsorption efficiency and electrochemical stability, resulting in superior cell performance.

The adsorption mechanism of the 1GO/9MWCNTs–COOH powders was further verified via ex situ XPS analysis (Figure 5c,d). Elemental comparisons before and after immersion tests revealed the emergence of two characteristic sulfur signals at 169 eV (S 2p) and 233 eV (S 1s) in the post-adsorption spectra (Figure 5d), demonstrating the successful adsorption of BNDTH species. Deconvolution of C 1s spectra (Figure S13, Supporting Information) identified five components: C–C/C=C (284.8 eV), C–S/C–O (285.8 eV), C=O (287.1 eV), O–C=O (289.1 eV), and π-π* (291.6 eV).[41] The intensified C–S signal after immersion further corroborates the chemical adsorption of BNDTH. High-resolution S 2p spectra (Figure 5d) revealed two doublet components: a primary pair at 164.4 ($2p_{3/2}$) and 165.8 eV ($2p_{1/2}$) corresponding to BNDTH's C–S–C bonds, and an additional sulfur doublet at 169.1 and 170.3 eV attributed to C–SO_x–C formation,[42,43] which likely arises from interactions between the sulfur atoms in BNDTH and the carboxyl groups in the carbon interlayer, forming chemically stable anchoring sites that suppress BNDTH diffusion. While both MWCNTs−COOH and Hummers-derived GO possess oxygen-containing functional groups such as −COOH (Figure S14, Supporting Information), their distribution and accessibility differ significantly. In Hummers-derived GO, these carboxyl groups are predominantly located at the sheet edges, resulting in limited interaction sites and insufficient adsorption capacity. As a consequence, GO alone exhibits negligible sequestration of BNDTH molecules when immersed in BNDTH-saturated DME solution, consistent with the persistent coloration observed in the macroscopic adsorption test (Figure 5a). In contrast, MWCNTs−COOH presents a more uniform distribution of accessible carboxyl groups across its surface, enabling stronger interactions with BNDTH and thus dominating the overall adsorption process. This conclusion is strongly supported by both spectroscopic evidence

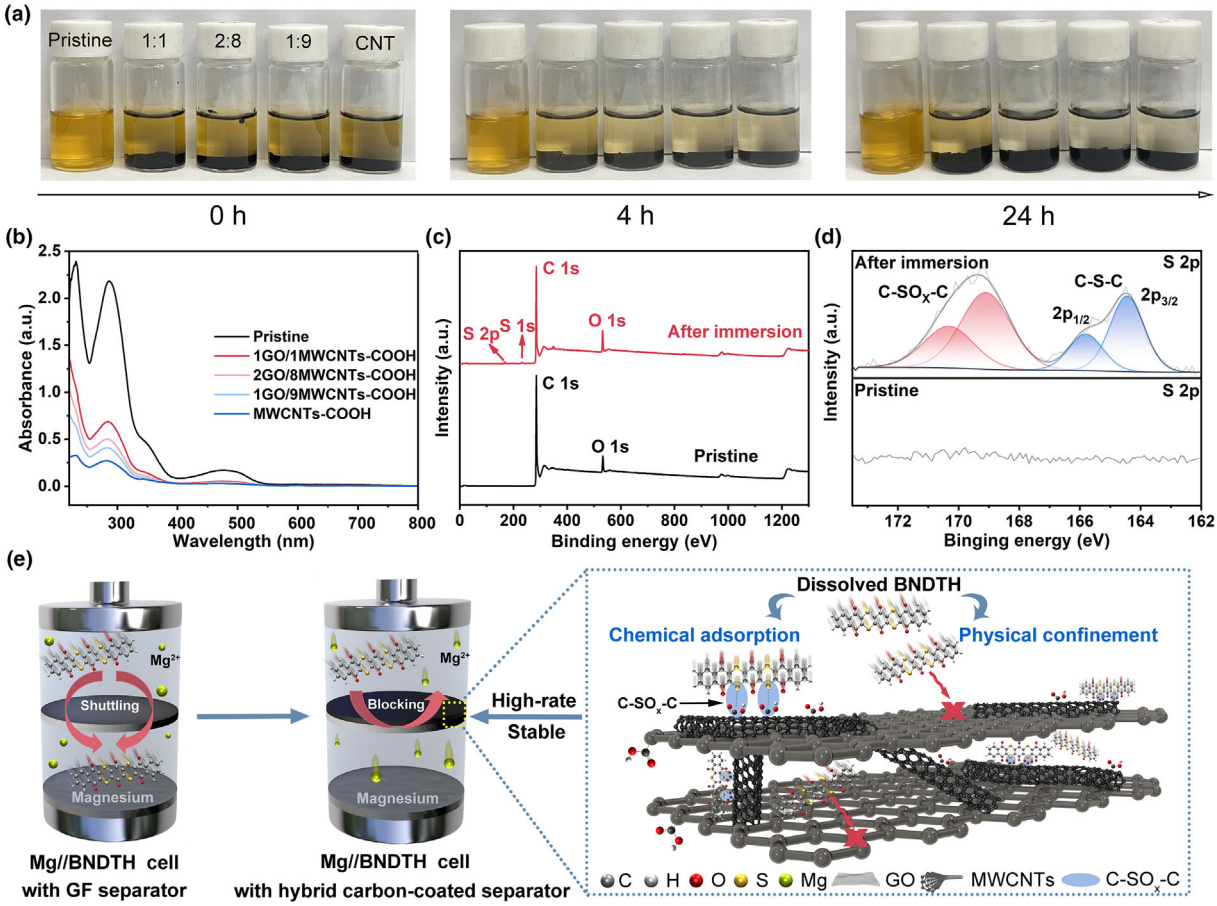

Figure 5. Investigation of the confinement–adsorption mechanism and schematic illustration. a) Optical photos of different mass ratios of GO/MWCNT−COOH immersed in saturated BNDTH/DME solution at different times. b) UV–vis spectra of the BNDTH/DME solution after different mass ratios of GO/MWCNTs−COOH immersing for 4 h. c) XPS spectra of 1GO/9MWCNTs−COOH hybrid carbon and d) S 2p XPS spectra before and after immersion in saturated BNDTH/DME solution. e) Schematic model illustrating the synergistic confinement–adsorption mechanism within the hybrid membrane.

and the comparative adsorption behavior among various carbon interlayers. The working mechanism of the GO/MWCNTs−COOH hybrid separator is illustrated in Figure 5e, highlighting a synergistic confinement–adsorption effect. In this configuration, GO nanosheets serve as physical barriers that confine the migration of dissolved molecules, while MWCNTs-COOH contribute abundant carboxyl functional groups that provide strong chemical adsorption sites. This dual mechanism operates cooperatively to immobilize dissolved BNDTH species, thereby mitigating active material loss and enhancing the cycling stability of the Mg//BNDTH cell.

3. Conclusion

In summary, the BNDTH was developed as a high-performance organic cathode material for RMBs. The CMC binder, among five different binders, was found to show good affinity with BNDTH, enabling the formation of robust cathode coating on the current collector. To address solubility-induced capacity fading of the BNDTH cathode, a hybrid carbon-coated separator was constructed using an optimized GO/MWCNTs−COOH mass ratio of 1:9. Within this architecture, the lamellar GO component provides effective physical confinement, while carboxyl-functionalized MWCNTs offer abundant chemical adsorption sites, enabling a synergistic confinement–adsorption mechanism to immobilize dissolved BNDTH species and mitigate their diffusion toward the Mg anode. When paired with this functional separator, the BNDTH cathode exhibited substantial capacity improvements, with reversible capacities increasing from 125 to 253 mAh g^{-1} (initial cycles) at 1 C and from 26 to 100 mAh g^{-1} at 10 C over 500 cycles. Moreover, the cell delivered a high-power density of 4517 W kg^{-1} while maintaining a considerable energy density of 222 Wh kg^{-1}. Ex situ FTIR and XPS analyses revealed a reversible enolization redox mechanism during magnesium storage of the BNDTH cathode, and the formation of C–SO_x–C moieties in the hybrid carbon coating was identified as key adsorption sites for dissolved BNDTH species. This work provides an effective strategy for stabilizing soluble small-molecule organic cathodes in RMBs and highlights the critical role of separator engineering in achieving high-rate and durable magnesium storage.

4. Experimental Section

Material synthesis: BNDTH was synthesized following established procedures.[31] Typically, a mixture of 2.3 g (10 mmol) of 2,3-dichloro-1,4-naphthoquinone and

1.8 g (23 mmol) of hydrated sodium sulfide in 100 mL deionized water was stirred and refluxed at 100 °C for 2 h. After cooling to 70 °C, 1.3 g (5.3 mmol) of tetrachlorobenzoquinone in 30 mL of N,N-dimethylformamide (DMF) was added, and the reaction was continued for another 4 h at 70 °C. The resulting solution was poured into 100 mL of ice water, and the pH was adjusted to 3–4 with a 5 wt% HCl solution. The precipitate was collected by filtration, thoroughly washed with ethanol, and dried under vacuum at 70 °C for 12 h. The final product was purified by recrystallization from DMF.

Preparation of GO/MWCNTs—COOH modified separator: GO was synthesized using Hummers' method as previously reported.[44] Commercial MWCNTs—COOH were obtained from Jiangsu XFNANO Materials Tech Co., Ltd. A series of hybrid coatings with a total carbon mass of 80 mg were prepared, in which the mass ratio of GO to MWCNTs–COOH was systematically varied and designated as 1GO/xMWCNTs—COOH. The detailed procedure for the representative 1GO/9MWCNTs–COOH modified separator is described as follows: First, 8 mg of GO was dispersed in 20 mL of ethanol by ultrasonication for 1 h. Then, 72 mg of MWCNTs–COOH was added to the homogeneous GO dispersion, and the mixture was further sonicated for 4 h to form a uniform slurry. The resulting slurry was vacuum-filtered onto a commercial glass fiber separator (Whatman GF/F), vacuum-dried at 70 °C for 8 h, and finally punched into 19 mm diameter disks for cell assembly.

Electrolytes preparation: First, 2.13 mL of HFIP-H was dissolved in 5 mL of DME in a 100 mL glass bottle, followed by the slow addition of 10 mL of 1 M $Mg(Bu)_2$ in heptane. The mixture was stirred continuously for 5 h. In parallel, 7.07 mL of HFIP-H was dissolved in 5 mL of DME in a 20 mL glass bottle, and 24.4 mL of BH_3-THF solution was added dropwise under stirring, after which the reaction was continued for 5 h. The two resulting solutions were then combined and stirred at room temperature for 12 h. The final product, $Mg[B(hfip)_4]_2$ salt, was obtained after vacuum drying at 60 °C for 24 h. The salt was subsequently dissolved in DME in a volumetric flask to prepare a 0.5 M electrolyte solution for electrochemical testing.

Materials characterization: XRD patterns were collected on a Rigaku SmartLab diffractometer using Cu-Kα radiation. FTIR spectroscopy was performed on a Thermo Nicolet Nexus 670 Spectrometer. Morphological analysis was carried out using FE-SEM (Carl Zeiss Microscopy GmbH). Chemical states of the constituent elements were analyzed by XPS on a Thermo Scientific instrument equipped with a monochromatic Al Kα X-ray source. All XPS spectra were calibrated by setting the adventitious carbon C 1s peak to a binding energy of 284.8 eV.

Electrode preparation: The cathode slurry was formulated by thoroughly mixing BNDTH (as the active material) and Ketjen black (as the conductive additive) with a selected binder at a mass ratio of 60:30:10. For aqueous processing, binders including CMC, SA, PAA, or LA133 were dissolved in deionized water. In the case of non-aqueous processing, PVDF was dissolved in N-methyl-2-pyrrolidone. The homogenized slurry was uniformly cast onto C–Al foil and dried under vacuum at 60 °C for 12 h. The resulting electrodes were then punched into 12 mm disks and paired with magnesium metal counter electrodes for cell assembly.

Electrochemical measurements: The electrochemical performance was evaluated using 2032-type coin cells assembled in an argon-filled glove box. The separators employed included GF, the 1GO/9MWCNTs–COOH modified separator, and other hybrid carbon-coated separators. Galvanostatic charge–discharge tests were carried out on a Neware battery test system (CT-4008T). CV was performed using a Bio-Logic VMP3 potentiostat. All measurements were conducted at 298 K.

Acknowledgements

This work was financially supported by the National Natural Science Foundation of China (NSFC, Grant Nos. 52222211 and 52472209), the State Key Laboratory of Materials-Oriented Chemical Engineering (Grant No. SKL—MCE—23A05), "333" Project of Jiangsu Province, and the Priority Academic Program Development of Jiangsu Higher Education Institutions (PAPD).

Conflict of Interest

The authors declare no conflict of interest.

Supporting Information

Supporting Information is available from the Wiley Online Library or from the author.

Keywords

confinement–adsorption synergy, hybrid carbon-coated separators, magnesium batteries, organic cathodes, quinone

Received: December 7, 2025
Revised: December 26, 2025
Published online: January 3, 2026

[1] Y. J. Li, S. Kumar, G. L. Yang, J. Lu, Y. Yao, K. Kang, Z. W. Seh, *Science* **2025**, *389*, eadl5482.
[2] Y. J. Li, X. Feng, G. L. Yang, W. Y. Lieu, L. Fu, C. Zhang, Z. X. Xing, M. F. Ng, Q. F. Zhang, W. Liu, J. Lu, Z. W. Seh, *Nat. Commun.* **2024**, *15*, 9364.
[3] H. Y. Fan, X. X. Zhang, J. H. Xiao, W. J. Chen, Q. Y. Lin, Z. S. Ng, Y. T. Lin, Y. Su, L. D. Pan, Y. P. Su, S. Y. Ren, H. W. Liu, X. Z. Li, Y. G. Zhang, *Energy Environ. Mater.* **2024**, *7*, e12792.
[4] J. L. Zhang, Z. H. Zhang, H. Zhou, J. Liu, A. B. Du, S. M. Dong, X. H. Zhou, Q. F. Wang, G. C. Li, G. L. Cui, *Adv. Mater.* **2025**, *37*, 2417652.
[5] J. Long, Z. He, G. Zhang, Y. Ding, J. Zhang, P. Liu, H. Xu, R. Wang, S. Tan, Q. An, L. Mai, *Adv. Mater.* **2025**, *37*, e10488.
[6] Y. P. Pang, Z. F. Nie, F. Xu, L. X. Sun, J. H. Yang, D. L. Sun, F. Fang, S. Y. Zheng, *Energy Environ. Mater.* **2024**, *7*, e12527.
[7] G. Y. Li, L. Cao, M. Lei, K. Y. Chen, C. L. Li, *Energy Environ. Sci.* **2025**, *18*, 7254.
[8] T. F. Wang, K. Y. Chen, G. Y. Li, Z. Chen, Y. F. Gao, C. L. Li, *ACS Nano* **2025**, *19*, 16877.
[9] K. J. Xu, X. Q. Qi, X. Y. Zhao, *Rev. Mater. Res.* **2025**, *1*, 100129.
[10] F. Zhang, N. Jiang, Z. Y. Gao, S. J. Sun, Z. Zhao-Karger, X. Y. Zhao, *J. Mater. Sci. Technol.* **2026**, *258*, 218.
[11] Y. L. Shen, K. J. Xu, Z. Zhao-Karger, X. Y. Zhao, *Energy Environ. Mater.* **2026**, *9*, e70124.
[12] Y. Zhao, S. Chen, M. Zhou, M. Pan, Y. Sun, D. Zhang, S. Zhang, Y. Wang, M. Li, X. Zeng, J. Yang, J. Wang, Y. NuLi, *ACS Nano* **2024**, *18*, 22356.
[13] D. Wu, F. Wang, H. Yang, Y. Xu, Y. Zhuang, J. Zeng, Y. Yang, J. Zhao, *Energy Storage Mater.* **2022**, *52*, 94.
[14] J. Tian, X. J. Zhou, Q. P. Wu, C. L. Li, *Energy Storage Mater.* **2019**, *22*, 218.
[15] W. Wang, Y. Jiang, Y. Yang, F. Xiong, S. Zhu, J. Wang, L. Du, J. Chen, L. Cui, J. Xie, Q. An, L. Mai, *ACS Nano* **2022**, *16*, 17097.
[16] J. Tian, D. P. Cao, X. J. Zhou, J. L. Hu, M. S. Huang, C. L. Li, *ACS Nano* **2018**, *12*, 3424.
[17] J. Zhang, Z. Chang, Z. Zhang, A. Du, S. Dong, Z. Li, G. Li, G. Cui, *ACS Nano* **2021**, *15*, 15594.
[18] H. Liu, R. H. Yu, X. Q. Luo, D. Wu, D. X. Wang, J. S. Wu, L. Zhou, J. P. Liu, J. L. Xia, *Energy Environ. Mater.* **2025**, *8*, e12785.
[19] H. Park, H. Kye, J. S. Lee, Y. C. Joo, D. J. Min, B. G. Kim, S. Y. Park, J. E. Kwon, *Energy Environ. Mater.* **2024**, *7*, e12694.
[20] Y. Z. Zhao, M. Zhou, X. Q. Zeng, J. Yang, J. L. Wang, Y. Nuli, *Adv. Funct. Mater.* **2025**, *35*, 2423533.
[21] X. Ren, D. Tao, S. Cui, T. Li, Y. Cao, F. Xu, *Energy Storage Mater.* **2023**, *63*, 102992.
[22] Y. Chen, M. C. Yang, W. Hu, T. Chen, J. Li, S. Wang, H. L. Jin, J. C. Wang, *Energy Environ. Mater.* **2025**, *8*, e12819.
[23] X. Song, X. Xue, H. Xia, L. Jin, A. Tao, Y. Wang, J. Liang, Y. Liu, P. Zhang, Z. Tie, Y. Long, Z. Jin, *Energy Storage Mater.* **2023**, *55*, 426.

[24] W. Ren, M. S. Ng, Y. Zhang, A. E. Lakraychi, Y. L. Liang, D. W. Feng, M. Lehmann, G. Yang, J. Jeevarajan, W. S. Tang, Y. Yao, *ACS Nano* **2025**, *19*, 5781.
[25] H. Dong, O. Tutusaus, Y. L. Liang, Y. Zhang, Z. Lebens-Higgins, W. L. Yang, R. Mohtadi, Y. Yao, *Nat. Energy* **2020**, *5*, 1043.
[26] Q. Guo, H. Xu, X. Chu, X. Huang, M. Yu, X. Feng, *Chem. Soc. Rev.* **2025**, *54*, 4035.
[27] J. Bitenc, T. Pavcnik, U. Kosir, K. Pirnat, *Materials (Basel)* **2020**, *13*, 506.
[28] B. Pan, J. Huang, Z. Feng, L. Zeng, M. He, L. Zhang, J. T. Vaughey, M. J. Bedzyk, P. Fenter, Z. Zhang, A. K. Burrell, C. Liao, *Adv. Energy Mater.* **2016**, *6*, 1600140.
[29] S. Bai, B. Kim, C. Kim, O. Tamwattana, H. Park, J. Kim, D. Lee, K. Kang, *Nat. Nanotechnol.* **2020**, *16*, 77.
[30] Y. Wu, X. Wang, F. Zhang, L. Hai, Q. Chen, C. Chao, A. Yang, Y. Sun, D. Jia, *Adv. Funct. Mater.* **2023**, *34*, 2309552.
[31] T. Sun, W. Zhang, Q. Nian, Z. Tao, *Nano Micro Lett.* **2023**, *15*, 36.
[32] B. Pan, D. Zhou, J. Huang, L. Zhang, A. K. Burrell, J. T. Vaughey, Z. Zhang, C. Liao, *J. Electrochem. Soc.* **2016**, *163*, A580.
[33] Y. Ding, D. Chen, X. Ren, Y. Cao, F. Xu, *J. Mater. Chem. A* **2022**, *10*, 14111.
[34] T. Bančič, J. Bitenc, K. Pirnat, A. Kopač Lautar, J. Grdadolnik, A. Randon Vitanova, R. Dominko, *J. Power Sources* **2018**, *395*, 25.
[35] A. B. Ikhe, N. Naveen, K.-S. Sohn, M. Pyo, *Electrochim. Acta* **2018**, *283*, 393.
[36] H. Dong, Y. Liang, O. Tutusaus, R. Mohtadi, Y. Zhang, F. Hao, Y. Yao, *Joule* **2019**, *3*, 782.
[37] X. Xue, R. Chen, X. Song, A. Tao, W. Yan, W. Kong, Z. Jin, *Adv. Funct. Mater.* **2020**, *31*, 2009394.
[38] M. Mao, Z. Lin, Y. Tong, J. Yue, C. Zhao, J. Lu, Q. Zhang, L. Gu, L. Suo, Y. S. Hu, H. Li, X. Huang, L. Chen, *ACS Nano* **2020**, *14*, 1102.
[39] L. Zhou, Q. Liu, Z. Zhang, K. Zhang, F. Xiong, S. Tan, Q. An, Y. M. Kang, Z. Zhou, L. Mai, *Adv. Mater.* **2018**, *30*, e1801984.
[40] P. Jing, H. Lu, W. Yang, Y. Cao, *Electrochim. Acta* **2020**, *330*, 135263.
[41] J. Choi, A. Jin, H. D. Jung, D. Ko, J. H. Um, Y. J. Choi, S. H. Kim, S. Back, S.-H. Yu, Y. Piao, *Energy Storage Mater.* **2022**, *48*, 325.
[42] F. Li, X. Qian, L. Jin, *ACS Sustain. Chem. Eng.* **2021**, *9*, 15469.
[43] Y. Wang, H. Wu, L. Huang, H. Zhao, Z. Liu, X. Chen, H. Liu, Y. Zhang, *Inorg. Chem.* **2018**, *57*, 7993.
[44] C. Zhang, S. Sun, K.-H. Xue, Y. Miao, X. Hu, X. Zhao, *J. Mater. Chem. A* **2024**, *12*, 24203.